New Measurement Resolves Key Astrophysical Fe XVII Oscillator Strength Problem: Supplemental Material

Steffen Kühn,[1,2,*] Charles Cheung,[3] Natalia S. Oreshkina,[1] René Steinbrügge,[4] Moto Togawa,[1] Sonja Bernitt,[1,5,6,7] Lukas Berger,[1] Jens Buck,[8] Moritz Hoesch,[4] Jörn Seltmann,[4] Florian Trinter,[9,10] Christoph H. Keitel,[1] Mikhail G. Kozlov,[11,12] Sergey G. Porsev,[11,3] Ming Feng Gu,[13] F. Scott Porter,[14] Thomas Pfeifer,[1] Maurice A. Leutenegger,[14] Zoltán Harman,[1] Marianna S. Safronova,[3] José R. Crespo López-Urrutia,[1] and Chintan Shah[14,1,†]

[1]*Max-Planck-Institut für Kernphysik, Saupfercheckweg 1, 69117 Heidelberg, Germany*

[2]*Heidelberg Graduate School of Fundamental Physics, Ruprecht-Karls-Universität Heidelberg, Im Neuenheimer Feld 226, 69120 Heidelberg, Germany*

[3]*Department of Physics and Astronomy, University of Delaware, Newark, Delaware 19716, USA*

[4]*Deutsches Elektronen-Sychrotron DESY, Notkestraße 85, 22607 Hamburg, Germany*

[5]*Institut für Optik und Quantenelektronik, Friedrich-Schiller-Universität Jena, Max-Wien-Platz 1, 07743 Jena, Germany*

[6]*Helmholtz-Institut Jena, Fröbelstieg 3, 07743 Jena, Germany*

[7]*GSI Helmholtzzentrum für Schwerionenforschung, Planckstraße 1, 64291 Darmstadt, Germany*

[8]*Institut für Experimentelle und Angewandte Physik (IEAP), Christian-Albrechts-Universität zu Kiel, Leibnizstr. 11-19, 24098 Kiel, Germany*

[9]*Institut für Kernphysik, Goethe-Universität Frankfurt am Main, Max-von-Laue-Straße 1, 60438 Frankfurt am Main, Germany*

[10]*Molecular Physics, Fritz-Haber-Institut der Max-Planck-Gesellschaft, Faradayweg 4-6, 14195 Berlin, Germany*

[11]*Petersburg Nuclear Physics Institute of NRC "Kurchatov Institute", Gatchina 188300, Russia*

[12]*St. Petersburg Electrotechnical University "LETI", Prof. Popov Str. 5, St. Petersburg, 197376, Russia*

[13]*Space Science Laboratory, University of California, Berkeley, CA 94720, USA*

[14]*NASA/Goddard Space Flight Center, 8800 Greenbelt Rd, Greenbelt, MD 20771, USA*

(Dated: August 24, 2022)

This Supplemental Material presents technical details of the experiment as well as extended tables from the data analysis and theory calculations.

I. EXPERIMENT

We show the general scheme of the experiment in Fig. 1. PolarX-EBIT is installed in the first focal position behind the monochromator-exit port at branch 1 of the PETRA III beamline P04. Its position is mechanically adjusted to ensure the best possible overlap with the narrow photon beam in increments of ≈ 20 μm, and checked daily. At the trap center, the highly charged ions are confined within a cylindrical volume of 18 mm length and ≈ 200 μm diameter, which the photon beam passes along the trap axis. Two windowless silicon-drift detectors with 80 and 150 mm^2 sensitive areas, respectively, are mounted side-on at mutually orthogonal directions.

* Corresponding author.
steffen.kuehn@mpi-hd.mpg.de
† Corresponding author.
chintan.shah@mpi-hd.mpg.de

A. Setup

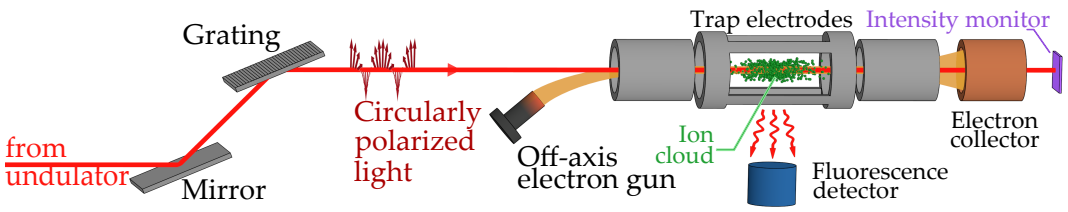

FIG. 1. Experimental setup. An off-axis electron gun injects an electron beam (orange) into the magnetic field of an electron beam ion trap. At its center, the electron beam generates highly charged ions, which are then trapped by the space-charge potential caused by the beam itself. The ions are then resonantly excited by a monochromatic, circularly polarized photon beam (red) at the PETRA III beamline P04. X-ray fluorescence due to the decay of the photoexcited states is registered by silicon-drift detector mounted side-on. The intensity of the photon beam is registered using an X-ray-sensitive diode downstream of the experimental setup. Figure adopted from [1].

B. Electron-beam energy switching cycle

In our last measurements [1], the Fe XVII target was produced by an electron beam at an energy of approximately 1600 eV. For the present measurement campaign, the measurement scheme uses a cycle including both an ion-breeding and a probing phase, see Fig. 2. During the ion-breeding phase, a sufficient amount of Fe XVII was produced by the electron beam at energies close to the values employed during the first measurement campaign. After this phase, the electron-beam energy was reduced to only 250 eV within a few ms for mitigating the background induced by both electron-impact excitation and dielectronic recombination. In this probing phase, the electron beam does not have enough energy to produce any undesired strong background signal in the photon-energy region around 800 eV. The beam energy during the probing phase was selected such that dielectronic recombination resonances, which have cross sections orders of magnitude larger than the direct radiative recombination were avoided as much as possible. However, the ions still experience radiative and charge exchange recombination. Due to these constant losses and the lack of any production channels for Fe XVII, the population of these ions is slowly depleted during the probing phase. After the Fe XVII population has almost entirely recombined during the probing phase, the cycle started over, and new ions were bred at the higher electron-beam energies; usually, hundreds of ms were required to produce enough Fe XVII. The lifetime of Fe XVII in the probing phase was usually in the order of tens to hundreds of ms, depending on several parameters such as electron-beam current, $Fe(CO)_5$ injection pressure, and residual gas pressure, as well as on the excitation of auto-ionizing transitions driven by the photon beam. Using the so-called magnetic-trapping mode, i. e., completely turning off the electron beam and radially confining the ion cloud purely by the magnetic field as demonstrated in [2, 3], was unfeasible for the PolarX-EBIT, since its magnetic field strength is several times lower than in superconducting EBITs, thus, the radial drift of the ion orbits increases too fast. Utilizing the breeding-probing scheme, the laser-induced fluorescence could be observed almost entirely background-free and thus, the signal-to-noise ratio could be improved by three orders of magnitude compared to the previous beamtime.

C. Measurement stability

We acquired the data presented in this paper within 16 hours, primarily during a night shift. Within this shift, no instabilities such as electron-beam current variations or beam dumps in the storage ring PETRA III, or $Fe(CO)_5$ injection-pressure variations in the PolarX EBIT were recorded. This experimental stability is reflected by constant amplitudes observed for both lines of Fe XVII 3C and 3D as well as B and C of Fe XVI, see left panel of Fig. 3. In the right panel of Fig. 3, the individual 3C/3D oscillator-strength ratio of 16 consecutive measurements as well as their weighted average (red) is depicted, resulting in a ratio of 3.51 with a statistical uncertainty of only 0.57%. The same stability is also found in the observed Lorentzian widths of all four lines, see Fig. 4, resulting in a statistical uncertainty ranging between 1% for 3C and 5% for 3D.

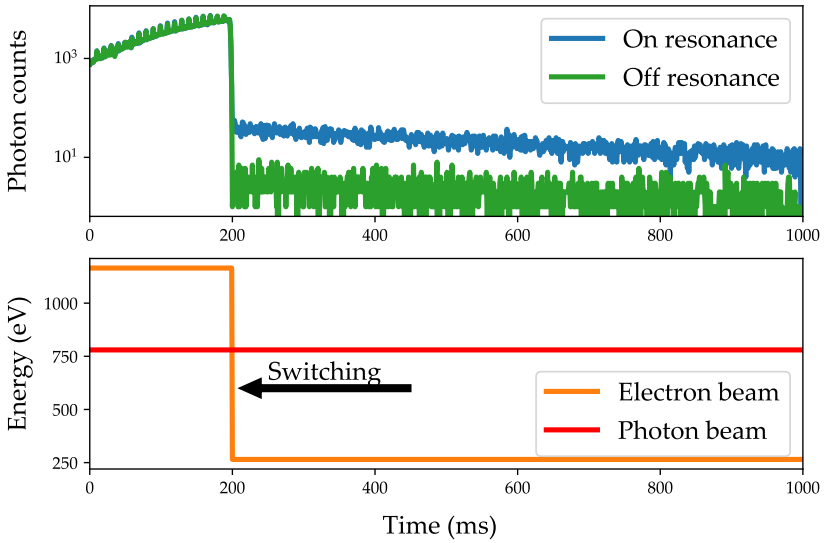

FIG. 2. Upper panel: Photon counts as a function of time during a measurement cycle. Highly charged ions are bred for 200 ms at an electron-beam energy of approximately 1200 eV (see orange curve in the bottom panel). After that, we switch it to a value well below any possible electron-impact-induced excitation channel. With the photon beam tuned on resonance 3C, a strong fluorescence signal is obtained (see blue curve in the upper panel). Note that during the breeding phase, the photon beam is unable to produce any sufficiently strong fluorescence signal that could be distinguished from the electron-impact-excited background.

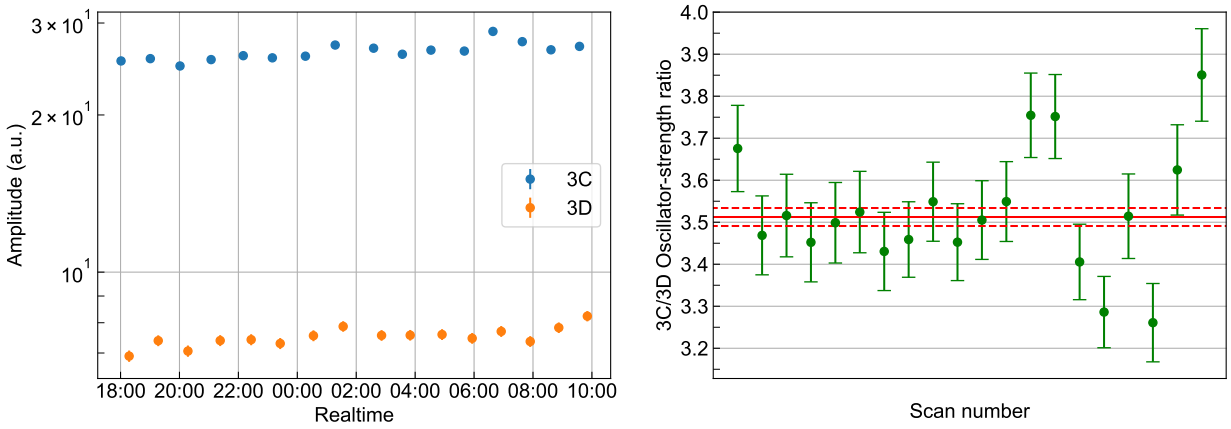

FIG. 3. Left panel: Observed amplitudes for 3C and 3D as a function of real time. Right panel: 3C/3D amplitude ratio for two consecutive scans of 3C and 3D lines. The red solid and dashed lines indicate the weighted average and statistical uncertainty.

D. Systematical uncertainties

1. *Region-of-interest selection*

One of the largest systematical uncertainties in our previous measurements presented in Ref. [1] arose from a poor signal-to-noise ratio (SNR) resulting in large variations of the final result depending on the selected region-of-interest (ROI) used to project the two-dimensional data to spectra. In this work, the SNR is by far sufficient to clearly separate the photon-beam-induced fluorescence signal from the electron-impact-induced background, see Fig. 5, completely eliminating any possible systematic uncertainties due to the ROI selection.

2. *Background and photon-flux instabilities*

In contrast to our previous measurements performed at P04, during this campaign a photodiode registering the incident photon-beam flux was mounted downstream of the experimental setup (see Fig. 1). Hence, the photon flux irradiating the trapped ion

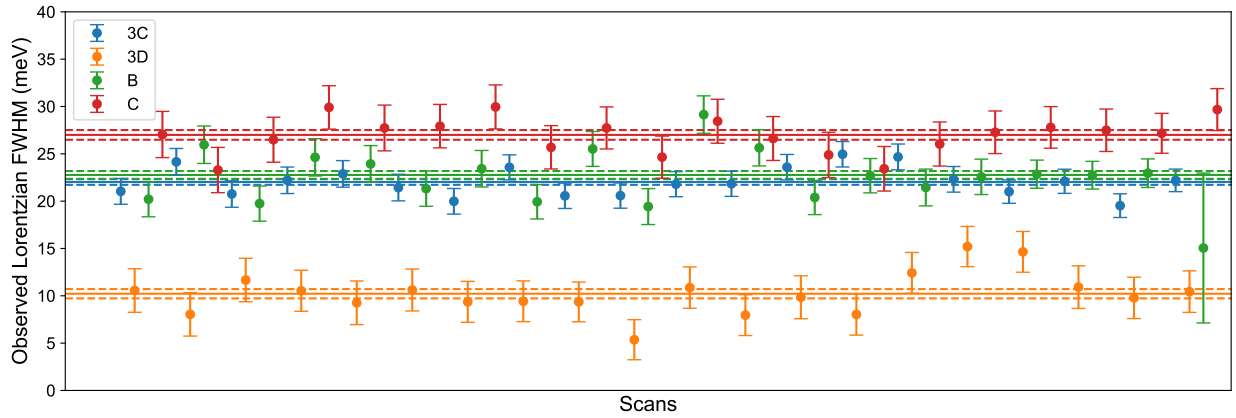

FIG. 4. Observed Lorentzian linewidths of the Voigt profiles applied to the measured fluorescence of the lines 3C (blue), 3D (orange), B (green), and C (red). The solid lines represent the weighted average of all measured linewidths of a given transition including the 1-σ deviation (dashed lines).

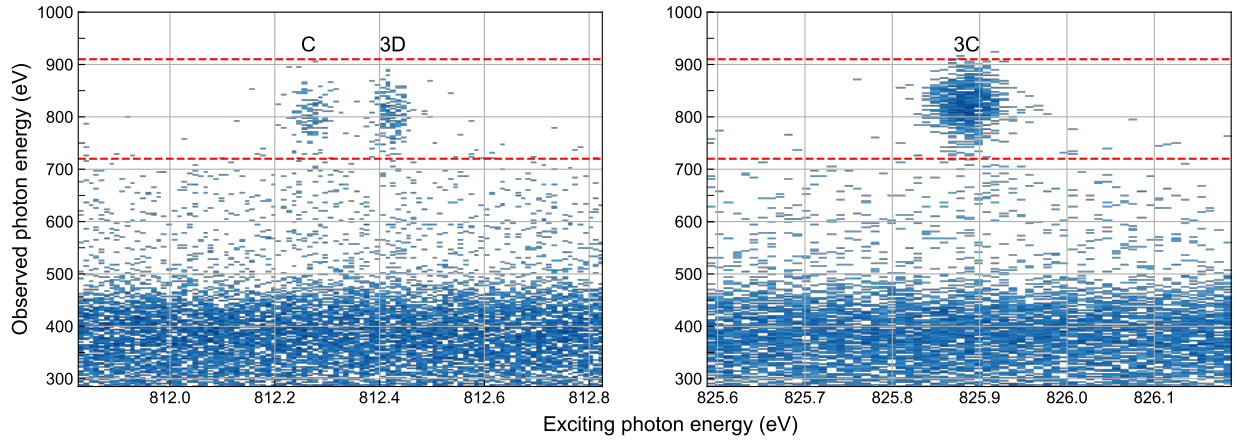

FIG. 5. Example of two-dimensional spectra of the trapped-ion emission spectrum as a function of exciting-photon energy. The high signal-to-noise ratio allows to clearly separate the fluorescence signal from the electron-beam-induced background. The regions-of-interest used for one-dimensional projections of the data are indicated by red dashed lines.

cloud was simultaneously monitored, and the observed line intensities accordingly corrected. Beside the expected 1% flux variation due to the top-up filling mode of the storage ring PETRA III and slight efficiency differences of the beamline due to energy-dependent X-ray-optic reflectivity, no anomalies were observed.

The stability of the ion-target production was continuously tracked by monitoring the electron-beam current, the $Fe(CO)_5$ injection pressure, and the low-energy background below 500 eV.

3. *Detection efficiency*

In front of both commercial windowless detectors used (Ketek Vitus H80 & Ketek Vitus H150), a 500 nm thick aluminum filter was employed to prevent visible light from saturating them. Since 3C and 3D have different energies, the filter transmission changes for each of them. We corrected the observed intensities based on literature values for the respective transmissions [4]. The thickness tolerance of the aluminum filter was specified within $\pm 10\%$. This results in an uncertainty of the transmission correction based on the literature values for 450 nm and 550 nm thick filters of approximately 0.13%. We assume a constant detector efficiency across the small energy range between 810 and 830 eV.

4. Non-linear effects

In order to explain the unexpectedly low value of the 3C/3D oscillator-strength ratio measured at LCLS, non-linear effects due to the high photon-flux peak intensity of the FEL were proposed [5, 6]. The radiative lifetimes of 3C and 3D are predicted to be 163 fs and 45 fs, respectively, and are thus in the same order of magnitude as the X-ray pulse lengths of LCLS of the experiment in Ref. [7] between 200 fs and 2000 fs [6]. It was hence proposed that the high flux of the free-electron laser was sufficient to populate the upper level of 3C and 3D at different rates within these short laser pulse.

According to Oreshkina *et al.* [5], a peak flux density of at least $1 \times 10^{12}\,\mathrm{W\,cm^{-2}}$ or more is required to observe such non-linear effects during the measurement. The photon peak intensity at the synchrotron beamline P04 is estimated based on the number of photons registered by the calibrated diode downstream of the experimental setup

$$\Psi_{\mathrm{Photonbeam}} = 4 \times 10^{11}\,\mathrm{photons/s}. \tag{1}$$

Given the employed monochromator energy of

$$E = 825\,\mathrm{eV} = 1.32 \times 10^{-16}\,\mathrm{J}, \tag{2}$$

an average power of

$$P_{\mathrm{average}} = 5.28 \times 10^{-5}\,\mathrm{W} \tag{3}$$

is obtained. During the measurements, PETRA III operated in timing mode, resulting in a photon-bunch repetition rate of $5.21 \times 10^{6}\,\mathrm{pulses/s}$. Combined with a minimal possible focal spot size of $1 \times 10^{-10}\,\mathrm{m^2}$ and a typical photon-bunch length of 44 ps, a peak flux density of

$$\rho \approx 2.3 \times 10^{9}\,\mathrm{W\,m^{-2}} \tag{4}$$

is obtained, which is orders of magnitude below the required value predicted by theories. It should be mentioned that the separation between two photon pulses of 192 ns was sufficiently long for the excited states of 3C and 3D, with lifetimes of tens to hundreds of fs, to decay to their ground states before the next photon pulse arrived. At the estimated photon peak flux and the long photon-pulse separation, non-linear effects of any kind, even for the most conservative assumptions of a minimal focus spot size and minimal bunch lengths, can be explicitly excluded for the measurements presented within this work.

5. Charge-state population transfer

After the ions were bred, the electron-beam energy was lowered to a fraction of the upper value to suppress background. Thereby, the lower electron-beam energy of 250 eV was no longer sufficient to produce the investigated charge states Fe XVI and Fe XVII. Due to recombination caused by interaction with the electron beam (radiative recombination) as well as with neutral residual gas (charge exchange), the population of highly charged ions was continuously depleted. The recombination rates of both charge states Fe XVII and Fe XVI were expected to be similar, but since Fe XVII recombined into Fe XVI, the latter was continuously fed resulting in an increasing Fe XVI/Fe XVII abundance ratio during the probing cycle obtained, as seen by comparing the areas of the lines C and 3D as a function of time, see Fig. 6. Since Fe XVII was the highest possible charge state produced during the breeding period, Fe XVII could not be produced by recombination from other, higher charge states.

In the LCLS measurements, the resolving power was insufficient to separate line 3D from C. Hence, it was proposed that the strong Auger-Meitner decay channel of the upper state of C to the ground state of 3D in Fe XVII combined with the high photon-flux intensity of the FEL caused a so-called population-transfer mechanism, i. e., a change of the plasma charge-state distribution during the measurements.

We investigated this effect in this work. The time evolution of the 3C/3D intensity ratio after switching down the electron-beam energy is depicted in Fig. 6. Even though the relative abundance of Fe XVI almost doubled during one probing cycle, the 3C/3D oscillator-strength ratio remained stable. To verify that the observed 3C/3D oscillator-strength ratio was constant and thus independent of the Fe XVI/Fe XVII abundance ratio, a linear model was fitted to the oscillator-strength ratio evolution. As expected, the fit agreed with a constant value. Hence, the 3C/3D oscillator-strength ratio was independent of the Fe XVI/Fe XVII abundance ratio, and charge-state population-transfer mechanisms are explicitly excluded.

6. Angular-encoder interpolation error

During an independent campaign performed at the PETRA III beamline P04 some months after the measurements presented here, we found that the angular encoder used to determine the grating rotation did not perform as expected. Unfortunately, we

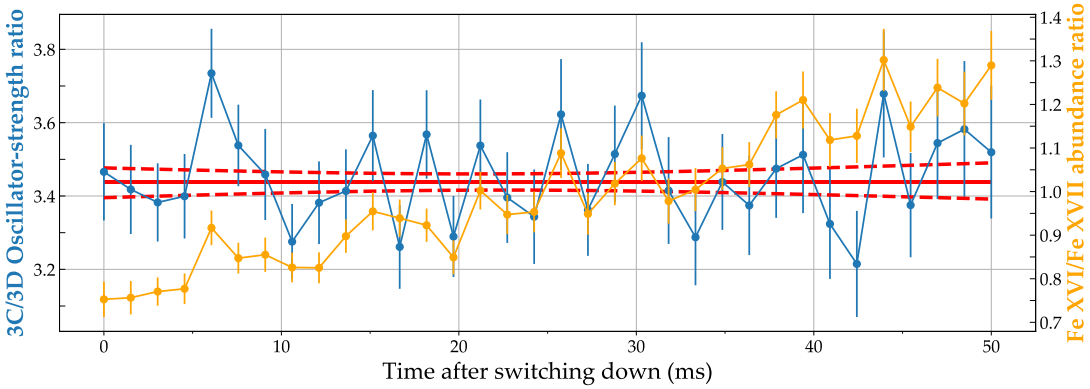

FIG. 6. Observed 3C/3D oscillator-strength ratio (blue, left axis) and the Fe XVI/Fe XVII abundance ratio (orange, right axis) as a function of time after switching down the electron beam. The red solid line shows the result of a linear function fitted to the oscillator-strength ratio values. Dashed lines indicate the 1-σ uncertainty.

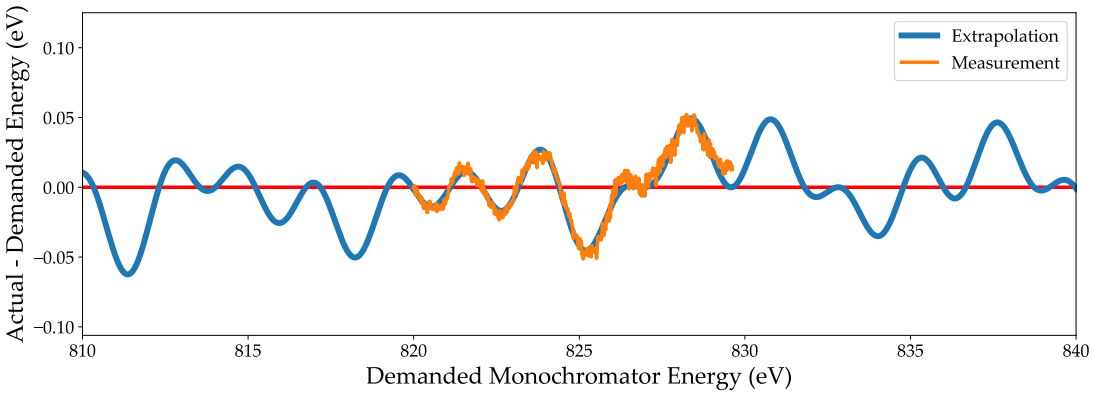

FIG. 7. Orange: measured difference between the actual and the demanded monochromator energy utilizing the ASPHERE III photoelectron spectrometer [8]. Blue: The acquired dataset is modeled and extrapolated using a combination of four sinusoidal waveforms.

found an oscillation distorting the monochromator photon-energy axis. The photon energy of the plane mirror, plane grating monochromator (PGM) at beamline P04 is calculated with the angles of the mirror and the grating measured by their corresponding rotary encoders. The encoder glass scales are segmented at regular intervals of 0.01 degrees, which relates, e.g., to $\approx$7 eV for the grating and $\approx$4.5 eV for the mirror (around 800 eV, fix focus constant $cff = 3.4$). A 14-bit interpolation is applied on the quadrature signals of each encoder. In principle, four photodiodes measuring the intensity transmitted between optical masks imprinted on the encoder disks capture periodically oscillating signals with different phases. Transforming these patterns into angular increments involves a careful and accurate intensity interpolation and normalization of the signal amplitudes of the different diodes. Measurements using the photoelectron spectrometer ASPHERE [8] located at P04 revealed periodic and reproducible departures with an amplitude of $\pm$40 meV from the otherwise (over large angular displacements) linear energy scale (see Fig. 7 of this Supplemental Material). A study of such angular calibration effects at the Swiss Light Source [9] showed that the interpolation errors typically did not interfere with measurements up to monochromator energy resolutions of $E/\Delta E \approx$10,000. However, in our present measurement, the effect is noticeable, since the encoder specifications of the P04 monochromator are different, and our resolution is twice as high.

The oscillations from Fig. 7 can be well described by a combination of four sinusoidal waveforms with periods of $\approx$1-2 eV around 800 eV, and are related to the aforementioned interpolation procedure. Recovering this accordion-like systematic periodic shift is in principle possible using the photoelectron spectrometer, since our statistical uncertainty in the line-centroid determinations is smaller than 1 meV. Unfortunately, such correction measurements were not performed here. Therefore, the influence of the periodic deviations on the oscillator-strength ratio had to be investigated by simulations. For this purpose, a synthetic periodic deviation of the photon energy consisting of the product of four sinusoidal waveforms was simulated, which in shape, amplitude, and periodicity approximately corresponded to the observed oscillations. Two synthetic Voigt profiles corresponding to the energies, amplitudes, and linewidths of 3C and 3D, respectively, were generated. Afterwards, each energy for which the intensities of the Voigt profiles were calculated was shifted by the simulated energy deviation. The shifted profiles were then analyzed using the same algorithms used for the analysis of the actual data, and the fit results were compared with the

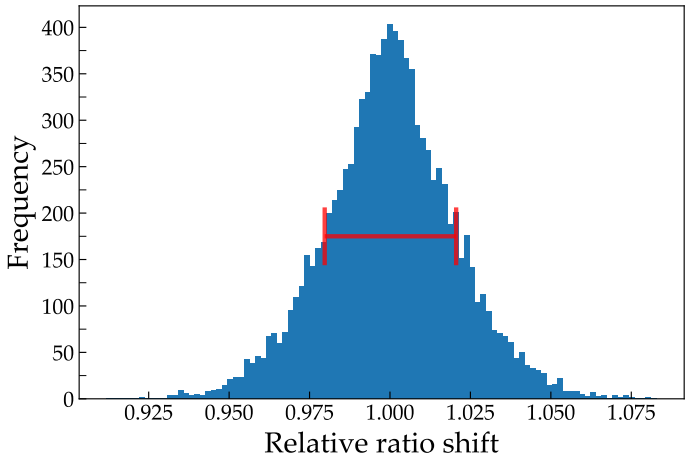

FIG. 8. Histogram of simulated relative shifts of the 3C/3D intensity ratio. Two synthetic Voigt lines were disturbed by simulated interpolation errors of the monochromator. The amplitudes of the disturbed lines were analyzed and compared with the initial parameters. Red bars represent the 1-σ standard deviation.

initial input parameters of the synthetic lines. In order to obtain an estimate of the distribution of the parameter changes, this simulation was performed 10000 times.

The relative change of the amplitude ratio due to simulated interpolation errors is depicted in Fig. 8. We find a distribution of the relative ratio shifts that is similar to a normal distribution centered at 1.0. Hence, on average, the ratio shift induced by incorrect energy interpolations is expected to be negligible. However, the periodic oscillations are assumed to be constant throughout the measurements for similar operating parameters, unless the correction tables of the angular encoders are changed. Hence, measurements of the same energy range will always result in the same oscillating deviation between the actual and the demanded photon energy. In order to assess this effect, the 1-σ standard deviation of the present simulation result of approximately 2% was added to the error budget of the final 3C/3D oscillator-strength ratio value. Using the same simulation program, the influence of this effect on the observed Lorentzian linewidths was also investigated and resulted in systematical uncertainties of up to 5% in the error budget of the natural linewidth determinations.

E. Error budget

The systematic and statistical uncertainties, as well as the final error budget of this work and of our previous measurement are listed in Tab. I.

TABLE I. Comparison of 3C/3D oscillator-strength ratio results including error budgets of Ref. [1] and this work.

Measurement	Kühn et al. 2020 [1]	**This work**
Number of scans (incl. B and C of Fe XVI)	6+11	60
Resolving power $E/\Delta E$ (FWHM)	8250	20000
Signal-to-noise ratio	≈ 0.05	≈ 45
Model used	Gaussian	Voigt
3C/3D oscillator-strength ratio	3.09	3.51
Statistical uncertainty	$\pm$2.58%	$\pm$0.57%
Systematical uncertainties		
ROI selection	$\pm$1.8%	X
Background instabilities	$\pm$1.0%	X
Area underestimation of Gaussian profiles fitted to Voigt lines	possible	excluded
Detection efficiency uncertainty	$\pm$0.13%	$\pm$0.13%
Monochromator interpolation errors	possible	$\pm$2.0%
Final 3C/3D oscillator-strength ratio	3.09(10)	**3.51(7)**

TABLE II. Measured natural linewidths and oscillator strengths from two independent methods. Both agree well with predictions.

Line	Experiment				Theory	
	Method 1		Method 2			
	Γ (meV)	$f-$value	Γ (meV)	$f-$value	Γ (meV)	$f-$value
Fe XVII 3C	15.27(247)	2.35(38)	15.02(119)	2.31(18)	14.740(10)	2.271(2)
Fe XVII 3D	4.22(68)	0.67(11)	3.22(79)	0.51(13)	4.030(20)	0.641(3)
Fe XVI B	16.42(301)	0.86(16)	15.77(126)	0.83(7)	14.426 [10]	0.760 [10]
Fe XVI C	20.52(380)	2.18(40)	20.00(149)	2.12(16)	23.103 [10]	2.454 [10]
Fe XVII 3C – 3D	10.92(175)				10.71(2)	

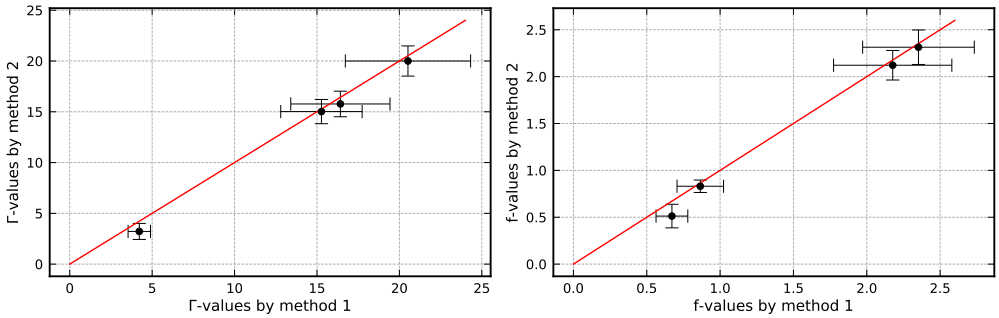

FIG. 9. Comparison between two methods extracting natural linewidths Γ (in meV) and oscillator strengths f-values for lines 3C, 3D, B, and C, respectively.

F. Natural linewidths and oscillator strengths determination

As described in the main manuscript, we determined the natural linewidths (Γ) for lines 3C, 3D, B, and C, respectively, with two independent methods. In the first method, we used the difference of Lorentz width between 3C and 3D lines and their intensity ratio to extract the absolute natural linewidths of measured transitions (see Eq. 1 and 2 of main manuscript). In the second method, the pseudo-Lorentzian part of the beam profile was first estimated using the F VIII w, K_β, and K_γ lines. Although the theoretical linewidths for He-like ions can be calculated very accurate, we conservatively used an error of 10% for the linewidths calculated from theory. Using these data, we estimated the Lorentzian instrumental contribution to be $\Gamma_{\text{beamline}} = 7.0 \pm 0.3$ meV.

On the other side, the thousandfold improvement of the SNR and the excellent 20000 spectral resolving power enabled us to extract the Lorentzian linewidths of the Voigt-like line shape of all four investigated lines 3C, 3D, B, and C with unprecedented small relative statistical uncertainties well below 10% for a single scan. The individual observed Lorentzian linewidths Γ' for the lines in each scan are shown in Fig. 4. Similar to the distribution of the observed 3C/3D oscillator strength ratio, all Lorentzian linewidth values appear to be statistically distributed. The values for the observed Lorentzian linewidths were obtained by taking the average of the individual measurements, weighted by their uncertainty.

$$\Gamma'_{3C} = 22.02(30)\,\text{meV},\ \Gamma'_{3D} = 10.22(49)\,\text{meV},\ \Gamma'_{B} = 22.77(41)\,\text{meV},\ \text{and}\ \Gamma'_{C} = 27.00(51)\,\text{meV},$$

In order to extract the pure natural linewidths Γ_{exp} of these transitions, we subtracted the beamline contribution Γ_{beamline} from above Γ' values. Table II represents the individual natural linewidths extracted for each line. Both independent values agrees well with our predictions.

Moreover, the oscillator strengths $f-$values of each measured transitions can be inferred using the relation between natural linewidth and oscillator strength that is as follows,

$$g_k\, f_{ki} = C\, \lambda_{ik}^2\, g_i\, A_{ik}, \tag{5}$$

where $C = 1/(32\,\pi^3\,\alpha\,a_0^2 Ry) = 1.499\,19 \times 10^{-14}$ nm^{-2}s. The g_i and g_k represent the statistical weights of initial state i and final state k, respectively. The λ_{ik} is a transition wavelength given in nanometers. A spontaneous transition rate A_{ik} represents the probability per unit time for an ion in any g_i state of energy level i to make transition to g_k state of the level k.

The derived oscillator strengths also agree well with the predictions, see Tab II. The consistency between extracted Γ and f values from two independent analysis methods is also shown in Fig. 9. Note that both analysis methods have a relative systematic uncertainty of 5% resulting from the periodic energy shifts of the monochromator, as described in Sect. I D 6.

II. THEORY: CALCULATION OF THE 3C/3D LINE-INTENSITY RATIOS OF Fe^{16+}

We start from the solution of the Dirac-Hartree-Fock equations in the central-field approximation to construct one-particle orbitals. These calculations are carried out using a configuration-interaction (CI) method, correlating all 10 electrons of the Ne-like ion and taking into account the Breit interaction in all calculations. QED effects are considered following the method outlined in Ref. [11]. During the procedure, basis sets of increasing sizes are used to check for convergence of the values. Each of these is designated by the highest principal quantum number of each partial wave included. As an example, the label [$12spdfg$] means that all orbitals up to $n = 12$ are included for the $spdfg$ partial waves. We compared two different methods of constructing the basis sets and found both leading to the same results. We also noticed that the inclusion of the $6-12h$ orbitals did not modify the results, and therefore, we omitted higher partial waves.

The CI many-electron wave function Ψ_n is obtained as a linear combination of all Slater determinants Φ_i of a given parity:

$$\Psi_n = \sum_i c_i \Phi_i \,.$$

The energies and wave functions are determined from the time-independent many-electron Schrödinger equation $H\Psi_n = E_n\Psi_n$. Contributions to the $E1$ reduced matrix elements $D(3D) = D(2p^6\ {}^1S_0 - 2p^5 3d\ {}^3D_1)$ and $D(3C) = D(2p^6\ {}^1S_0 - 2p^5 3d\ {}^1P_1)$ and the ratio of the respective oscillator strengths

$$R(3C/3D) = \left(\frac{D(3C)}{D(3D)}\right)^2 \times \frac{\Delta E(3C)}{\Delta E(3D)}$$

are calculated and listed below.

We start with all possible single and double excitations to any orbital up to $12spdfg$ from the $2s^22p^6$, $2s^22p^53p$, $2s2p^63s$, $2s^22p^54f$ even and $2s^22p^53s$, $2s^22p^53d$, $2s2p^63p$, $2s^22p^54s$, $2s^22p^54d$ odd configurations, correlating 8 electrons.

Contributions to the energies of Fe XVII are calculated and listed in Table III. The results are compared with a revised analysis of tabulated experimental data [12]. We use LS coupling and NIST data term designations for comparisons but note that jj coupling would be more appropriate for this ion. Contributions to the $D(3C)$ and $D(3D)$ $E1$ reduced matrix elements and the $3C/3D$ ratio are listed in Table IV, respectively. The $3C/3D$ energy ratio is 1.01654. We find $R = f_{3C}/f_{3D} = 3.55 \pm 0.02$.

We include additional configurations obtained by excitations from the $1s^2$ shell to the $6-12h$ orbitals and list them as "$1s^2$" and "$12h$" in Tables III and IV. The contributions from the $1s^2$ shell improve the agreement with the experiment for energies, but have only a very small (-0.006) effect on f_{3C}/f_{3D}. Inclusion of the $6-12h$ orbitals gives negligible corrections to both energies and matrix elements. Contributions from triple excitations were also found to be negligible in a previous calculation [1], and we did not recalculate them here. We expand the basis set from [$12spdfg$] to [$17spdfg$], and then to [$24spdfg$], and find a modest improvement of the energies compared to the experiment, but a very small shift of R by -0.003. The last line of Table III shows the difference of the $3C$ and $3D$ energies in eV, with the final value being $3C - 3D = 13.44$ eV.

As an independent test of the quality and completeness of the current basis set, we compare the results for $D(3C)$ and $D(3D)$ obtained in length and velocity gauges for the [$12spdfg$] basis, see rows L and V in Table IV. The difference in the results is only 0.001. Calculations were also done using a completely different B-spline basis set at the level of [$17spdfg$], with energy differences of no more than 0.03% between the two basis sets, with energies of the B-spline basis set further away from experimental values. The value of the ratio R differed by 0.0064 between the two basis sets.

We have also compared different QED potentials described in Ref. [11]. All QED corrections in Tables III and IV were calculated with the QEDMOD variant (see Ref. [11]). We found negligible maximum energy differences of -7 cm^{-1}, -13 cm^{-1}, and 3 cm^{-1}, between the different potentials. Compared to the semi-empirical approach, there was a maximum energy difference of 94 cm^{-1}. The energy difference was negligible in each comparison.

Transition rates of all other transitions contributing to the radiative decay of the $3C$ and $3D$ levels were also calculated. The totals of these rates are small and listed in Table IV. The linewidth value corresponds to the total transition rate.

TABLE III. Contributions to the energies of Fe^{16+} calculated with increased-size basis sets and number of configurations. The results are compared with experiment. All energies are given in cm^{-1} with exception of the last line that shows the difference of the $3C$ and $3D$ energies in eV. The basis set is designated by the highest quantum number for each partial wave included. For example, $[12spdfg]$ means that all orbitals up to $n = 12$ are included for $spdfg$ partial waves.

Configuration		Expt. [12]	$[12spdfg]$	$+1s^2$	$+[12h]$	$+[17spdfg]$	$+[24spdfg]$	QED	Final	Diff. [12]	Diff. [12]
$2s^22p^6$	$^1S_0$	0	0	0	0	0	0	0	0	0	0
$2s^22p^53p$	$^3S_1$	6093295	6090490	200	-2	933	480	70	6092171	1124	0.02%
$2s^22p^53p$	$^3D_2$	6121484	6118934	217	-5	861	433	56	6120496	988	0.02%
$2s^22p^53p$	$^3D_3$	6134539	6131883	210	-4	881	447	107	6133524	1015	0.02%
$2s^22p^53p$	$^1P_1$	6143639	6141023	218	-5	865	432	93	6142626	1013	0.02%
$2s^22p^53s$	2	5849216	5845504	429	-1	884	453	813	5848082	1134	0.02%
$2s^22p^53s$	1	5864502	5860927	371	-2	854	435	814	5863400	1102	0.02%
$2s^22p^53s$	1	5960742	5956909	415	-2	868	444	1067	5959702	1040	0.02%
$2s^22p^53d$	$^3P^o_1$	6471640	6468748	313	-14	864	487	95	6470492	1148	0.02%
$2s^22p^53d$	$^3P^o_2$	6486183	6483425	314	-16	858	485	109	6485176	1007	0.02%
$2s^22p^53d$	$^3F^o_4$	6486720	6484084	319	-19	830	481	105	6485800	920	0.01%
$2s^22p^53d$	$^3F^o_3$	6492651	6490106	319	-20	813	475	102	6491795	856	0.01%
$2s^22p^53d$	$^1D^o_2$	6506537	6503970	317	-21	831	478	107	6505682	855	0.01%
$2s^22p^53d$	$^3D^o_3$	6515203	6512722	314	-21	806	469	107	6514396	807	0.01%
$2s^22p^53d$	$^3D^o_1$	6552503	6550091	293	-22	812	474	151	6551800	703	0.01%
$2s^22p^53d$	$^3F^o_2$	6594309	6591493	355	-20	839	485	355	6593507	802	0.01%
$2s^22p^53d$	$^3D^o_2$	6600998	6598052	348	-19	845	485	349	6600060	938	0.01%
$2s^22p^53d$	$^1F^o_3$	6605185	6602336	354	-21	818	478	363	6604328	857	0.01%
$2s^22p^53d$	$^1P^o_1$	6660770	6658398	249	-25	802	473	299	6660196	574	0.01%
$3C-3D$ (eV)		13.4234	13.4283	-0.0055	-0.0004	-0.0012	-0.0001	0.0183	13.4395	-0.0161	-0.12%

TABLE IV. Contributions to the E1 reduced matrix elements $D(3D) = D(2p^6\ ^1S_0 - 2p^53d\ ^3D_1)$ and $D(3C) = D(2p^6\ ^1S_0 - 2p^53d\ ^1P_1)$ (in a.u.) and the ratio of the respective oscillator strengths R. See caption of Table III for designations. L and V rows compare results obtained in length and velocity gauges for the $[12spdfg]$ basis. All other results are calculated using the length gauge. Transition rates and linewidth are listed at the bottom of the table. Total of the other transition rates contributing to the lifetime of the 3C and 3D levels are listed in row "Other transitions".

		$D(3C)$	$\Delta D(3C)$	$D(3D)$	$\Delta D(3D)$	$R(3C/3D)$	ΔR
$[12spdfg]$	L	0.33523		0.17883		3.572	
	V	0.33546		0.17893		3.573	
	$+1s^2$	0.33505	-0.00018	0.17889	0.00006	3.566	-0.006
	$+[12h]$	0.33523	0.00000	0.17884	0.00001	3.572	0.000
$[17spdfg]$		0.33522	-0.00001	0.17889	0.00006	3.570	-0.002
$[24spdfg]$		0.33520	-0.00002	0.17890	0.00001	3.569	-0.001
QED			-0.00013		0.00033		-0.016
Final		0.33489		0.17930		3.546	
Recommended transition rate (s^{-1})		$2.238(2)\times10^{13}$		$6.11(2)\times10^{12}$			
Other transitions (s^{-1})		1.49×10^{10}		1.38×10^{10}			
Total rate (s^{-1})		$2.239(2)\times10^{13}$		$6.12(2)\times10^{12}$			
Linewidth (meV)		**14.74(1)**		**4.028(15)**			

TABLE V. Comparison of the oscillator-strength ratio f_{3C}/f_{3D} and natural linewidths of 3C and 3D between this work, available experimental datasets, and a selection of theoretical predictions. If available, n_{Config} corresponds the number of included configurations in the calculation. Additionally, the employed method of each measurement or calculation is given: EIE (electron-impact excitation), RSXES (resonant soft-X-ray excitation spectroscopy), DW (distorted wave), RM (R-Matrix), MBPT (many-body perturbation theory), MCDF (multi-configuration Dirac-Fock), CI (configuration interaction), BP-CI (Breit-Pauli configuration interaction). Note that the validity of theory published by Mendoza *et al.* [13] has been disputed [14]. All linewidths and linewidth differences are given in meV FWHM.

	Method	f_{3C}/f_{3D}	$\Gamma_{3C}-\Gamma_{3D}$	Γ_{3C}	Γ_{3D}	n_{Config}
This work	**RSXES**	**3.51(7)**	**10.92(175)**	**15.07(107)**	**3.79(52)**	
Experiments						
Brown (2001) [15]	EIE	1.90(11) - 3.04(12)				
Beiersdorfer (2004) [16]	EIE	2.04(42) - 3.33(56)				
Brown (2006) [17]	EIE	2.98(30)				
Gillaspy (2011) [18]	EIE	1.96(14) - 2.78(11)				
Bernitt (2012) [7]	RSXES	2.61(23)				
Kühn (2020) [1]	RSXES	3.09(10)				
Astrophysical observations						
Blake (1965) [19]		1.63				
McKenzie (1980) [20]		2.75				
Mewe (2001) [21]		2.42				
Behar (2001) [22]		3.02				
Xu (2002) [23]		2.31(18)				
Ness (2003) [24]		2.73(57)				
Astrophysical models and databases						
NIST ASD [25]	–	3.66	11.25	15.20	3.95	./.
AtomDB 3.0.9 [26]	–	3.90	12.18	16.19	4.01	./.
SPEX 3.0.6 [27]	–	4.05	12.10	15.89	3.79	./.
Chianti 10.0.2 [28]	–	4.07	12.10	15.86	3.76	./.
Theoretical work						
Zhang et al. (1989) [29]	DW	4.15	12.38	16.15	3.77	./.
Bhatia et al. (1992) [30]	RM	3.74	13.64	17.38	3.74	37
Cornille et al. (1994) [31]	DW	4.52	12.63	16.07	3.44	65
Kaastra et al. (1996) [27]	RM	3.84	13.89	17.73	3.84	./.
Safronova et al. (2001) [32]	MBPT	3.43	10.49	14.63	4.14	36
Dong et al. (2003) [33]	MCDF	4.26	10.92	15.18	4.26	20257
Loch et al. (2005) [34]	CI	3.91	12.18	16.19	4.01	189
Chen et al. (2007) [35]	Dirac RM	3.43	10.63	14.81	4.18	./.
Gu (2009) [36]	DW	4.03	12.33	16.23	3.90	./.
Gu (2009) [36]	MBPT	3.50	10.19	14.09	3.90	./.
Jönsson et al. (2014) [37]	CI	3.56	10.73	14.74	4.01	700000
Santana et al. (2015) [38]	CI	3.68-3.96	11.58	15.71	4.13	816
Santana et al. (2015) [38]	MBPT	3.44	10.30	14.34	4.04	7
Oreshkina et al. (2016) [10]	CI	3.55	10.65	14.61	3.96	100000
Mendoza et al. (2017) [13]	BP-CI	2.82	9.95	15.14	5.19	./.
Wu et al. (2019) [39]	MCDF	3.48	10.58	14.66	4.08	3.7×10^6
Wu et al. (2019) [39]	MCDF+Breit	3.56	10.75	14.76	4.01	3.7×10^6
Kühn et al. (2020) [1]	MCDHF	3.55(5)	10.72	14.74(3)	4.02(6)	1.2×10^6
Kühn et al. (2020) [1]	CI	3.55(5)	10.72	14.74(3)	4.02(5)	230000
Kühn et al. (2020) [1]	CI+MBPT (AMBiT [40])	3.59(5)	10.86	14.90	4.04	1×10^6
Gu (2021) [41]	CI	3.49	10.50	14.52	4.02	./.
This work	**CI**	**3.55(2)**	**10.71(2)**	**14.74(1)**	**4.03(2)**	$\mathbf{1.2\times10^6}$

[1] S. Kühn, C. Shah, J. R. Crespo López-Urrutia, K. Fujii, R. Steinbrügge, J. Stierhof, M. Togawa, Z. Harman, N. S. Oreshkina, C. Cheung, M. G. Kozlov, S. G. Porsev, M. S. Safronova, J. C. Berengut, M. Rosner, M. Bissinger, R. Ballhausen, N. Hell, S. Park, M. Chung, M. Hoesch, J. Seltmann, A. S. Surzhykov, V. A. Yerokhin, J. Wilms, F. S. Porter, T. Stöhlker, C. H. Keitel, T. Pfeifer, G. V. Brown, M. A. Leutenegger, and S. Bernitt, Phys. Rev. Lett. **124**, 225001 (2020).

[2] P. Beiersdorfer, R. Olson, G. Brown, H. Chen, C. Harris, P. Neill, L. Schweikhard, S. Utter, and K. Widmann, Phys. Rev. Lett. **85**, 5090 (2000).

[3] V. Mäckel, R. Klawitter, G. Brenner, J. R. Crespo López-Urrutia, and J. Ullrich, Phys. Rev. Lett. **107**, 143002 (2011).

[4] B. Henke, E. M. Gullikson, and J. C. Davis, At. Data Nucl. Data Tables **54**, 181 (1993).

[5] N. Oreshkina, S. M. Cavaletto, C. H. Keitel, and Z. Harman, Phys. Rev. Lett. **113**, 143001 (2014).

[6] S. D. Loch, C. P. Ballance, Y. Li, M. Fogle, and C. J. Fontes, Astrophys. J. **801**, L13 (2015).

[7] S. Bernitt, G. V. Brown, J. K. Rudolph, R. Steinbrügge, A. Graf, M. Leutenegger, S. W. Epp, S. Eberle, K. Kubiček, V. Mäckel, M. C. Simon, E. Träbert, E. W. Magee, C. Beilmann, N. Hell, S. Schippers, A. Müller, S. M. Kahn, A. Surzhykov, Z. Harman, C. H. Keitel, J. Clementson, F. S. Porter, W. Schlotter, J. J. Turner, J. Ullrich, P. Beiersdorfer, and J. R. Crespo López-Urrutia, Nature **492**, 225 (2012).

[8] K. Rossnagel, L. Kipp, M. Skibowski, and S. Harm, Nucl. Instrum. Methods Phys. Res., Sect. A **467-468**, 1485 (2001), proceedings of the 7th Int. Conf. on Synchrotron Radiation Instru mentation.

[9] J. Krempaský, R. Follath, V. N. Strocov, T. Schmitt, and U. Flechsig, in *Advances in X-Ray/EUV Optics and Components VI*, Vol. 8139, edited by C. Morawe, A. M. Khounsary, and S. Goto, International Society for Optics and Photonics (SPIE, 2011) pp. 176 – 180.

[10] N. S. Oreshkina, S. M. Cavaletto, C. H. Keitel, and Z. Harman, J. Phys. B: At., Mol. Opt. Phys. **49**, 094003 (2016).

[11] I. I. Tupitsyn, M. G. Kozlov, M. S. Safronova, V. M. Shabaev, and V. A. Dzuba, Phys. Rev. Lett. **117**, 253001 (2016).

[12] A. Kramida, Preliminary critical analysis of Fe XVII spectral data, Private Communication (2019).

[13] C. Mendoza and M. A. Bautista, Phys. Rev. Lett. **118**, 163002 (2017).

[14] K. Wang, P. Jönsson, J. Ekman, T. Brage, C. Y. Chen, C. F. Fischer, G. Gaigalas, and M. Godefroid, Phys. Rev. Lett. **119**, 189301 (2017).

[15] G. Brown, P. Beiersdorfer, H. Chen, M. Chen, and K. Reed, Astrophys. J. Lett. **557**, L75 (2001).

[16] P. Beiersdorfer, M. Bitter, S. Von Goeler, and K. Hill, Astrophys. J. **610**, 616 (2004).

[17] G. V. Brown, P. Beiersdorfer, H. Chen, J. H. Scofield, K. R. Boyce, R. L. Kelley, C. A. Kilbourne, F. S. Porter, M. F. Gu, S. M. Kahn, and A. E. Szymkowiak, Phys. Rev. Lett. **96**, 253201 (2006).

[18] J. Gillaspy, T. Lin, L. Tedesco, J. N. Tan, J. M. Pomeroy, J. Laming, N. Brickhouse, G.-X. Chen, and E. Silver, Astrophys. J. **728**, 132 (2011).

[19] R. Blake, T. Chubb, H. Friedman, and A. Unzicker, Astrophys. J. **142**, 1 (1965).

[20] D. McKenzie, P. Landecker, R. Broussard, H. Rugge, R. Young, U. Feldman, and G. Doschek, Astrophys. J. **241**, 409 (1980).

[21] R. Mewe, A. Raassen, J. Drake, J. Kaastra, R. Van Der Meer, and D. Porquet, Astron. Astrophys. **368**, 888 (2001).

[22] E. Behar, J. Cottam, and S. Kahn, Astrophys. J. **548**, 966 (2001).

[23] H. Xu, S. Kahn, J. Peterson, E. Behar, F. Paerels, R. Mushotzky, J. Jernigan, A. Brinkman, and K. Makishima, Astrophys. J. **579**, 600 (2002).

[24] J. Ness, J. Schmitt, M. Audard, M. Güdel, and R. Mewe, Astron. Astrophys. **407**, 347 (2003).

[25] A. Kramida, Yu. Ralchenko, J. Reader, and and NIST ASD Team, NIST Atomic Spectra Database (ver. 5.9), [Online]. Available: `https://physics.nist.gov/asd` [Mon Jun 20 2022]. National Institute of Standards and Technology, Gaithersburg, MD. (2022).

[26] A. R. Foster, L. Ji, R. K. Smith, and N. S. Brickhouse, Astrophys. J. **756**, 128 (2012).

[27] J. S. Kaastra, R. Mewe, and H. Nieuwenhuijzen, in *11th Colloq. on UV and X-ray Spectroscopy of Astrophysical and Laboratory Plasmas*, edited by K. Yamashita and T. Watanabe (Universal Academy Press, Tokyo, 1996) pp. 411–414.

[28] G. Del Zanna, K. P. Dere, P. R. Young, and E. Landi, Astrophys. J. **909**, 38 (2021), arXiv:2011.05211 [physics.atom-ph].

[29] H. L. Zhang and D. Sampson, At. Data Nucl. Data Tables **43**, 1 (1989).

[30] A. Bhatia and G. Doschek, At. Data Nucl. Data Tables **52**, 1 (1992).

[31] M. Cornille, J. Dubau, and S. Jacquemot, At. Data Nucl. Data Tables **58**, 1 (1994).

[32] U. I. Safronova, C. Namba, I. Murakami, W. R. Johnson, and M. S. Safronova, Phys. Rev. A **64**, 012507 (2001).

[33] C. Dong, L. Xie, S. Fritzsche, and T. Kato, Nucl. Instrum. Methods Phys. Res., Sect. B **205**, 87 (2003).

[34] S. Loch, M. Pindzola, C. Ballance, and D. Griffin, J. Phys. B: At., Mol. Opt. Phys. **39**, 85 (2005).

[35] G. Chen, Phys. Rev. A **76**, 062708 (2007).

[36] M. Gu, arXiv e-prints (2009).

[37] P. Jönsson, P. Bengtsson, J. Ekman, S. Gustafsson, L. B. Karlsson, G. Gaigalas, C. F. Fischer, D. Kato, I. Murakami, H. A. Sakaue, H. Hara, T. Watanabe, N. Nakamura, and N. Yamamoto, At. Data Nucl. Data Tables **100**, 1 (2014).

[38] J. A. Santana, J. K. Lepson, E. Träbert, and P. Beiersdorfer, Phys. Rev. A **91**, 012502 (2015).

[39] C. Wu and X. Gao, Scientific Reports **9**, 7463 (2019).

[40] E. V. Kahl and J. C. Berengut, Comput. Phys. Commun. **238**, 232 (2019).

[41] M. F. Gu, Calculations of the 3C/3D and 4C/4D oscillator-strength ratios of Fe^{16+} and Ni^{18+}. Private Communication (2021).